JOURNAL OF GEOPHYSICAL RESEARCH, VOL. , NO. , PAGES 1–33,

Magnitude and variance of horizontal heat flux at the Main Endeavour hydrothermal vent field

Scott R. Veirs, Russell E. McDuff, Frederick R. Stahr

School of Oceanography, University of Washington, Seattle, WA, USA

S. R. Veirs School of Oceanography, University of Washington, Box 357940, Seattle, WA 98195, USA. (scottv@ocean.washington.edu)

R. E. McDuff School of Oceanography, University of Washington, Box 357940, Seattle, WA 98195, USA. (mcduff@ocean.washington.edu)

F. R. Stahr School of Oceanography, University of Washington, Box 357940, Seattle, WA 98195, USA. (stahr@ocean.washington.edu)

Abstract. We characterize hydrothermal plume hydrography with unprecedented resolution using data acquired within the axial valley of the Endeavour segment, Juan de Fuca ridge, northeast Pacific, by an autonomous underwater vehicle (the Autonomous Benthic Explorer), a lowered CTD, and 2 current meter moorings. Our survey of the Main Endeavour hydrothermal vent field (MEF) shows hydrographic variability on unexpectedly short scales of ∼20 m and ∼10 min. Northward mean flow of 2–5 cm/s within the confines of the valley enables us to estimate a mean horizontal heat flux in the bottom ∼100 m despite variability induced by tidal oscillations with ∼5 cm/s amplitude. The mean northward transport implies that fluid entrained by plumes in the MEF is best characterized at the southern boundary of the field where the observed mean temperature anomaly is ∼0.05°C, an important result for a companion study that quantifies the vertical heat flux from the field. Differences in temperature anomaly north and south of the MEF, combined with the mean flow, lead to a net along-axis horizontal heat flux with a mean magnitude of ∼65 MW. An advection/diffusion model forced by nearby current data explains the variability in the observed temperature field and indicates that the variance of the mean horizontal flux is high (standard deviation ∼100 MW). A steady state MEF heat budget, constrained by the observed horizontal flux and measurements of vertical fluxes from other studies has 2 implications: the MEF heat flux is partitioned about equally between diffuse and focused vents, and about 4/5 of diffuse plumes are entrained by focused plumes.

1. Introduction

Within the axial valley of the Endeavour segment in the northeast Pacific (Figure 1), currents near the Main Endeavour field (MEF) consistently exhibit a mean northward flow (∼1-5 cm/s) superimposed on tidal oscillations of comparable amplitude [*Franks*, 1992; *Veirs et al.*, 1999; *Thomson et al.*, submitted, 2002]. Similar combinations of tidal and mean flows have been observed near hydrothermal sites within the axial valleys of other oceanic ridges [*Keller et al.*, 1975; *Thurnherr*, 2000].

When such flows distribute tracer from a source enclosed by a control volume, the net outward flux of tracer through the boundaries can vary significantly over time. In the case of a hydrothermal vent field, even if the source heat flux is constant, nearby temperatures can change quickly as thermal energy pools within the volume during slack flow periods and streams outward through the perimeter during peak cross flow. Attempts to measure the total flux through the boundaries can result in a time series that has surprisingly high variance and, depending on how temperature and velocity signals are averaged, a mean magnitude dramatically different from the source magnitude [*Wetzler et al.*, 1998].

Hydrothermal plumes from diverse types of vents are embedded in the flow at MEF. A key parameter that determines the fate of these plumes is their source buoyancy flux,

$$B = \frac{g(\rho - \rho_o)}{\rho_o} Q, \tag{1}$$

which depends on the density of the vented fluid (ρ) and the volume flux at the vent (Q), as well as two constants: the acceleration due to gravity ($g = 9.8$ m/s^2) and a reference density ($\rho_o \sim 10^3$ kg/m^3). The vent fluid temperature (T) and salinity (S) are the primary controls on ρ, while Q is simply the product of the source area (A) and the venting velocity (w).

Plumes from low B ("diffuse") MEF sources are expected to equilibrate relatively close to the valley floor ($\lesssim$100 m above source, hereafter abbreviated "mas") (J.W. Lavelle, NOAA/PMEL, pers. comm.). For comparison, plumes from high B ("focused") sources, like MEF black smokers, typically have rise heights of 100–300 mas [*Speer and Rona*, 1989; *Middleton and Thomson*, 1986]. Unlike high B plumes that rise above the ridge crests to be advected away, the low-lying plumes contain thermal and chemical energy with less certain fate. Their distribution may be controlled by entrainment into nearby plumes from high buoyancy flux sources, by lateral transport in ambient currents, or by a combination of both. Each possibility has distinct implications for the design of flux measurements and the dispersal of vent larvae and microbes.

The Flow Mow experiment (August 3–21, 2000) was designed to measure the advective heat flux through both the top and sides of a control volume enclosing all known MEF hydrothermal sources (Figure 1). The vertical flow of hydrothermal plumes rising through the top control surface was surveyed in a back and forth pattern (mowed) by the autonomous underwater vehicle Autonomous Benthic Explorer (ABE). Estimates of the vertical heat flux through this upper surface are presented in *Stahr et al.* [submitted, 2002]. The side surfaces were surveyed repetitively during the experiment with ABE or a navigated CTD with the intent of calculating the net horizontal heat flux. Motivated by the predominance of along-axis motions in a 1995 current record acquired near the MEF and close to the sea floor, we focused on monitoring the north and south sides. Meanwhile, near-bottom currents were recorded at 2 moorings located ∼1.1 km north and south of the field (Figure 1).

This paper begins with a description of the Flow Mow experiment, its setting, and instrumentation. We then highlight the differences between the regional background and hydrothermally-influenced hydrography. After summarizing current records from within the axial valley, we present temperature anomaly measurements made north and south of the MEF. We combine the temperature and current data sets to estimate the net horizontal heat flux through the sides of the MEF control volume. Subsequently, we use a simple advection-diffusion model to interpret the observed flux magnitudes and gain insight into the flux variance expected near the MEF. Finally, we discuss the implications of the horizontal heat flux estimates for the calculation of vertical flux and the partitioning of heat flux between distinct types of hydrothermal sources within the MEF.

2. The Flow Mow experiment

2.1. Setting

The topography and hydrography of the Endeavour segment present a distinct opportunity to measure heat fluxes. The vertical relief of the axial valley (∼100 m) is greater than the rise height of diffuse plumes, but less than the rise height of focused plumes. The top of the axial valley also marks a change in currents — from strong and rotary flow above the ridge crests to relatively weak and rectified flow within the axial valley. Thus, the topography and currents motivate different methodologies for measuring heat flux within the axial valley versus above it. Above the ridge crests, flux measurements depend on interception of advected plumes [e.g. *Baker and Massoth*, 1987]. This approach is required at fast spreading centers where the axial caldera is typically too shallow to constrain hydrothermal plumes. In contrast, a typical slow spreading center has a deep axial valley that can confine hydrothermal plumes [e.g. *Rudnicki et al.*, 1994] and motivates a budgetary approach to quantifying fluxes [*Murton et al.*, 1999] and diapycnal diffusivities [*Thurnherr et al.*, 2002]. The Flow Mow experiment was designed to intercept plumes within the Endeavour axial valley, accounting both for equilibrated plumes moving horizontally near the bottom and for buoyant plumes rising out of the valley, but not yet exposed to the overlying flow.

The Endeavour segment is essentially a short linear ridge with an elongate summit depression, or axial valley, that is open at both ends, but shoals to a sill near the north end (Figure 1). When defined by the 2170 m isobath (the depth of the sill) the east and west crests of the segment are ∼10 and ∼12 km long, respectively. At the latitude of the MEF, the segment is ∼4 km wide when measured between the points where the outer flanks rise abruptly from adjacent depressions that are 2350–2400 m deep. The rounded outer flanks rise about 250 m to crests near 2100 m depth.

Tectonic spreading at a half rate of 29 mm/yr [*Elvers et al.*, 1973] has created an axial valley that has a uniform width of ∼1 km between the rims [*Kappel and Ryan*, 1986]. Near the MEF the valley floor is ∼500 m wide and is bounded by basaltic talus slopes and/or fault scarps. Analysis of segment bathymetry shows that these valley walls have an average relief of ∼100 m and slopes of 10-30°. Along-axis, the valley floor shoals to the north at an average rate of ∼18 m/km. Like the other known fields to the north and south (see Figure 1 for names), the MEF rests on the relatively flat valley floor where basaltic sheet and pillow flows are intermittently broken by along-strike fissures that are 10–100 cm wide and normal faults with typical throws of 1-10 m.

While the major fields are separated along-strike with spacing of ∼2 km [*Delaney et al.*, 1996], a growing number of high and low B sources have been located or are suspected in-between (Figure 1) [*Veirs et al.*, 1999; *Johnson et al.*, 2002; *Kelley et al.*, 2002]. Of particular importance to this study is a low B area ∼500 m south of MEF called Quebec. This area is roughly 40 m square, rich in tube worm beds venting ∼12°C fluid, and potentially close enough to the MEF to exert an influence on measurements of horizontal heat flux through the south side of the MEF control volume.

The MEF is the most thoroughly mapped hydrothermal area on the Endeavour segment, having been the subject of myriad Alvin dives (more than any other site in the world) and numerous geophysical surveys. The field consists of 2 clusters of sulfide structures separated by ∼150 m along-strike (020° true). Most structures are based on basalt near 2195 m depth and are 3-21 m tall. While some structures in the north rest as deep as 2205 m, and a few in the south have bases as shallow as 2190 m, source depths are similar throughout the field because the 7 major northern structures are distinctly larger than the ∼11 southern structures. Based on elevation and dimensions in the map of *Delaney et al.* [1992], the active sulfide structures in the north have larger diameters (20–40 m versus 10–20 m in the south) and are taller on average (∼12±4 m versus ∼7±2 m). Consequently, the average depth of MEF high B sources is about the same in the north and south clusters (2185±6 m versus 2188±5 m).

Within the MEF, the top and side surfaces of the active sulfide structures may act as low B vents with areas up to 20–30 m in diameter. Tube worm patches, typically 2–10 m in extent, constitute low B fluid sources on the sea floor, either abutting sulfide structures or distributed along faults near sulfide structures. The maximum vertical separation of

MEF sources is 38 m — between a high B source, the 21 m high chimney at 2174 m on Dante, and a low B source, a tube worm bed at 2212 m just southwest of Crypto. More typical separations are $\lesssim$1 m between sulfide top surfaces and high B vents, and 10–15 m between tube worm beds and nearby black smokers.

The spatial distribution of distinct hydrothermal sources within the MEF is important for measuring fluxes because it guides the sizing of a control volume that encloses all sources in the field and intercepts all hydrothermal plumes ideally. The perimeter of the Flow Mow control volume (Figure 1) is a rectangle aligned with the strike of the valley. With a width of ∼300 m and a length of ∼700 m, it encompasses all the known MEF hydrothermal sources with a buffer of $\gtrsim$100 m. The top surface of the volume is a horizontal (constant pressure) plane ∼80 mas, an altitude near which the signal strength of rising plumes and the likelihood of intercepting them are simultaneously optimized [*Stahr et al.*, submitted, 2002]. The vertical surfaces of the control volume were surveyed from the top surface (∼2110 m) to within 5–10 m of the local sea floor (as deep as ∼2210 m).

2.2. Instrumentation

Hydrographic data were collected with pumped and ducted Sea Bird Electronics conductivity and temperature (CT) sensors mounted either within a lowered cage or in free flow on the front of ABE. In addition to deriving potential temperature (θ) and S from redundant CT sensor pairs, the lowered CTD recorded pressure, transmissivity, optical backscatter, fluorescence, oxygen concentration, redox potential, and cage altitude. An acoustic altimeter enabled ABE to monitor its elevation and avoid contact with the sea floor.

For the lowered hydrographic sensors, pre- and post-cruise calibrations did not differ significantly. Raw 24 Hz data were bin averaged to 0.5 Hz. The 0.5 Hz series were hand-edited for non-hydrothermal outliers and the resulting gaps were filled through linear interpolation. Processing of data from the ABE-mounted CT sensors is detailed in [*Stahr et al.*, submitted, 2002].

The hydrographic observations were located through long-baseline acoustic navigation whenever only one platform (CTD cage or ABE) was submerged. Only at stations >5 km from the MEF did the long baseline navigation degrade. When both platforms were submerged simultaneously, only ABE was navigated to preclude multiple interrogations of the transponders. In these instances, the CTD cage locations were estimated from the R/V Thompson GPS fixes, the ship heading, and the geometric relation between the block on the CTD boom and the ship GPS antenna. Comparison of CTD long-baseline and ship GPS fixes during similarly slow tows ($\lesssim$10 cm/s) indicates that the CTD rarely deviated laterally more than 10 m from the tip of the boom that supported it. All fixes were edited for outliers and interpolated onto the 0.5 Hz hydrographic time base.

Currents were recorded during the experiment by Aanderaa RCM5 instruments moored $\sim$1.1 km north and south of the MEF. Each current meter generated hourly mean speed and direction. The north mooring consisted of 2 RCM5s, 14 and 15 meters above bottom (mab). We use data exclusively from the shallower meter (2161 m depth) because the deeper meter failed prior to the beginning of the Flow Mow experiment. The south mooring supported 5 current meters at 50 m intervals (from 50–250 mab), but in this study we focus only on the lowest meter (2142 m depth) because its depth was comparable to that of the north meter and central to the Flow Mow control volume depth range (2100–2200 m).

Additional current observations were made with Nobska Modular Acoustic Velocity Sensors (MAVS). One MAVS was mounted on ABE during the experiment. Others were placed within the MEF by collaborating scientific programs and recorded near-bottom ($\lesssim$1 mab) velocity for short periods during the Flow Mow experiment. Data from the latter instruments have provided useful comparisons (courtesy of M. Tivey, S. Hautala, I. Garcia-Berdeal, and their associates).

2.3. Hydrographic context and anomaly definition

Current meters deployed *above* the ridge crests during the Flow Mow experiment and previous Endeavour segment studies show that the regional mean flow is $\sim$5 cm/s to the southwest. Although tidal and inertial oscillations are amplified in this depth range (1900–2100 m) [*Thomson et al.*, submitted, 2002], neither is capable of displacing hydrothermal plumes more than a few km from their axial sources. Consequently, we assume that vertical CTD casts acquired 10 and 15 km due east of the MEF prior to the experiment define the regional hydrographic context, or "background" for the Flow Mow experiment. The more distant station was at 47°57.01'N, 128°54.02'W, while the closer station was at 47°56.99'N, 128°58.02'W.

In particular, we assume that these upstream stations define the condition of the northeast Pacific deep water prior to topographic and hydrothermal influences. Like past casts taken at similar distances east of the axis, these stations display a near-linear θ–S trend and constant (clear water) transmissivity or backscatter signals over the depths where Endeavour hydrothermal plumes typically equilibrate (1700–2300 m). We calculate an *isohaline* potential temperature anomaly ($\Delta\theta$), using as a reference a 2nd-order polynomial fit to the near-linear θ–S background data (10-m depth-binned average of both stations). This is an important and strategic choice because the plume temperature anomaly reference (density, salinity, or depth) affects the relationship between source heat flux and the vertical flux measured in the rising plume [*McDougall*, 1990; *McDuff*, 1995; *Lavelle et al.*, 1998; *McDougall and Speer*, 1999; *Thurnherr*, 2000]; the relationship also depends on the S and θ of the source and entrained fluid, as well as whether the measurement is in zero or non-zero B parts of the plume. Through examination of a 1-dimensional plume model [*Morton*, 1959; *Speer and Rona*, 1989; *McDuff*, 1995], we find that isohaline $\Delta\theta$ requires the smallest correction ($\lesssim$5% at 100 mas) for plumes originating from sources with near-zero S anomalies, like the diffuse sources found in the MEF that have source $S \approx 99\%$ seawater S [*Veirs*, 2003]. This low correction factor motivates us to use isohaline $\Delta\theta$ to define the plume temperature anomalies.

Approaching from the east, hydrothermal influence on the θ–S trend first becomes evident on the outer ridge flank [*Veirs et al.*, 1999]. Above 2100 m on the southeast flank (only about 1 km southeast of the MEF) water properties are nearly indistinguishable from the background stations. Below 2100 m, the water is slightly above background in θ–S space, but less so than at any more central axial station. Similarly, a station taken on axis, but at the extreme north end of the segment, $\sim$15 km north of MEF, reveals no departure from the background trend over a wide range of depths (1700–2250 m). In contrast, axial stations located over or between the vent fields always sample fluid that has positive $\Delta\theta$ and high backscatter, indicating hydrothermal plume influence [*Veirs*, 2003]. Above and near ridge crest depth, background water is interspersed with layers of this plume water that vary in depth and thickness between sequential casts that are typically 0.3 hr apart or offset by $\sim$100 m. In this upper layer (1850–2100 m), stations taken $\lesssim$1 km southwest (downstream with respect to the regional mean current) of known fields tend to be the most anomalous. The intermittent returns to the background in this depth range (as well as below plume depths in distal downstream casts) assure that the near-linear background relationship can be extended, rather than extrapolated, through equilibrated plumes, as well as the axial valley depths.

Within the axial valley ($\gtrsim$2100 m) near MEF, water with background θ–S character is extremely rare. The $\Delta\theta$ of near-bottom fluid is almost always positive and generally increases along-axis toward the center of hydrothermal activity. In θ–S space, a profile within the valley typically plots parallel to, but above the background *Veirs* [2003].

2.4. Axial valley currents

Northward mean flows were observed within the axial valley both north and south of the MEF in 2000, and near the northeast corner of the MEF in 1995 (see Figure 1 for mooring locations and mean vectors). The magnitudes of the mean flow increase from south to north (1.6, 2.3, 4.7 cm/s), while the meter elevation decreases (50, 25, 15 mab). Similar south-to-north acceleration of mean flow was measured at the same locations during a 2001 deployment in which all meters were 15–17 mab; an additional 2001 record from further north (just south of the 2170 m saddle) showed a mean flow that was to the south at 1–2 cm/s [*Thomson et al.*, submitted, 2002]. Each of the records in 2000 and 2001 covered about 4 summer months, approximately from July through October.

The most prominent oscillation in the axial valley currents is at the M_2 semidiurnal frequency. At all depths on all moorings deployed in 2000 and 2001 the semidiurnal frequency band, dominated by the M_2, but also including the S_2 component, accounts for a greater proportion of the variance than any other constituent (low- or high-, inertial, or diurnal frequencies); and within 100 m of the bottom it consistently accounts for more than 50% of the total variance [*Thomson et al.*, submitted, 2002]. The vertical array of meters on the southern mooring reveals that the M_2 tidal ellipse has major axes that diminish from ∼4 cm/s at and above the ridge crest to 2–3 cm/s within the valley [*Thomson et al.*, submitted, 2002]. Consequently, along-axis flow reversals occur often at the south meter, where the oscillatory amplitude commonly exceeds the mean flow, and rarely at the north meter (Figure 2). At the 1995 meter, the combination of mean and oscillatory flow is intermediate, as is the intermittence of southward net fluid motion.

Before calculating and modeling horizontal heat fluxes through the MEF control surfaces, it is important to justify the local application of near-bottom currents measured at moorings up to 1.1 km away. Each mooring supported a meter near 2150 m, the central depth of the Flow Mow control volume. Auto- and cross-spectral analysis of the north and south meters reveals that there is statistically significant coherence and at most a +20° phase difference at the dominant (semidiurnal) frequency; the south meter (50 mab) leads the north meter (15 mab) by ∼45 min.

There is also evidence of general coherence in Figure 2 in which similar tidal oscillations combine with different northward mean flows at the north and south meters. In these 65 hr records, the magnitude of the mean flow relative to the amplitude of the tidal oscillations determines whether flow reversals occur. This short time series characterizes how rarely fluid is advected southward in the axial valley. Review of progressive vector diagrams (PVDs) generated with the longer records confirms that northward transport predominates at both meters throughout the Flow Mow experiment. On the other hand, the PVDs reveal a discrepancy between the 2 meters. North of the MEF, an eastward component of flow generates a mean direction parallel to the strike of the valley, while at the south meter a westward component results in a mean flow headed due north (Figure 1). A likely explanation for these opposite cross-axis components is that the moorings landed in distinct topography. The north meter was next to the western wall of the valley and likely experienced currents aligned with the 020° strike. The south mooring was centered in the valley and may have been influenced by westward flow over ∼2160 m saddle in the adjacent eastern ridge crest. The 1995 mooring was also centered in the valley and recorded a westward, albeit less persistent and strong, component of flow.

That near-bottom currents are approximately in phase is reinforced by a few short records of the flow that were acquired *within* the MEF during the Flow Mow experiment. Figure 3 juxtaposes the zero-mean, along-axis component of near-bottom flow from the north and south moorings with 3 different time series: the flow predicted through harmonic analysis of the 1995 data (H. Mofjeld, pers. comm.); the record from a MAVS deployed by M. Tivey in the center of MEF; and the ambient current measured with the MAVS mounted on ABE during 2 of the longest dives. We note that the 3rd series was calculated by subtracting ABE velocity, derived from navigational fixes of ∼1 m accuracy, from the ABE-mounted MAVS readings. That this method resolved the ambient current at all is a tribute to both the MAVS, the stability of the ABE platform, and the long baseline navigation system. During this characteristic 65 hr period (the same as in Figure 2), the ∼12 hr semidiurnal oscillations are approximately in phase. Most zero-crossings of the de-meaned records fall within ±1 hr of the predicted flow reversals.

The consistency of the mean flow and the spatial coherence of tidal oscillations within the axial valley flow justifies 2 strategies in this paper. First, the northward mean velocities that we combine with temperature data to calculate a range of observed fluxes will be bounded by the observed means (∼1–5 cm/s) from the north and south meters. Second, we elect to use a spring–neap cycle of the 1995 harmonic analysis to model MEF heat fluxes.

3. Observed flux magnitude

A fundamental assumption in the Flow Mow experimental design was that hydrographic conditions near the MEF control surfaces would be uniform. In a steady flow field, thermal homogeneity on the scale of the MEF would guarantee that advection of heat in one side of the field would be balanced by advection out the opposite side. Additionally, any heat entrained by plumes rising within the control volume could be accounted for by subtracting the mean $\Delta\theta$ observed on the perimeter from that observed on the top.

Contrary to our expectations, hydrographic surveys in the MEF and within ±500 m along-axis show that near-bottom variability is high. Upon spatial and temporal averaging, however, an overall pattern emerges: near the bottom it is warmer north of the MEF than south of it.

3.1. MEF $\Delta\theta$ fields

The $\Delta\theta$ fields on the north and south sides of the MEF control volume were observed during 3 separate ABE dives (45, 46, and 50) and are presented in Figure 4. Each panel overlays the ABE track line on $\Delta\theta$ data collected over a period of 2-3 hours. The data were subsequently projected orthogonally onto the north or south control surface for spatial averaging. The averaging bins (Δx =10 m, Δz =25 m) were designed to capture at least 2 ABE passes, obtaining $\gtrsim$100 points/bin. Dives 45 and 50 have north sides that are warmer on average than south sides, as expected, while dive 46 has a warmer south side, even when only the upper 50 m of the 2 sides are compared (means of 0.077°C versus 0.074°C).

Figure 4 also shows a higher spatial variability than anticipated. On any given pass along the 300 m wide side, plumes or thermal patches as narrow as 20 m were traversed. Sequential passes along the same side, sometimes separated only 10 m vertically and $\sim$10-20 min temporally, commonly encountered $\Delta\theta$ that varied by a factor of 2.

An additional perspective on the north and south side $\Delta\theta$ fields is gained through 3 vertically oscillating tows (VOTs), depicted in Figure 5. These data were projected in the same way, and averaged in bins (Δx =100 m, Δz =5 m) that encompassed at least 2 adjacent casts, or $\gtrsim$40 data points. During station 10, the CTD traversed the north side 3 times; the south side was surveyed $\sim$5.5 times during stations 12 and 13. While the south sides are uniformly warm in their upper 25 m, their lowest 25-50 m are variable and generally cooler than the same depth range on the north side. In the sequential panels of Figure 5, the first north side has the highest mean $\Delta\theta$, but many of the south sides are warmer than the second and third north sides. When sides are sorted into north and south groups and averaged, however, the mean south side (0.0677°C) is slightly cooler than the mean north side (0.0690°C).

The mean northward flow indicated by the 1995 current meter motivated us to place special emphasis during the Flow Mow experiment on comparing 2 CTD survey areas (dubbed "NoMEF" and "SoMEF") that extended $\sim$500 m along-axis north and south of the MEF boundary (Figure 1). Both areas were monitored intermittently during distinct tidal phases, and toward the end of the experiment were reoccupied for longer, near-tidal periods. NoMEF was monitored for about 10 hours during a vertically oscillating cast (VOC) between 1800 and 2200 m (station 28). A few days later, SoMEF was assessed (~200 m west of previous SOMEF stations) for 14 hr during a VOC between 1800 and 2150 m (station 33). Figure 6 portrays the evolution of the $\Delta\theta$ field in the NoMEF and SoMEF areas, with averaging bins again designed to capture at least 2 adjacent casts (Δt =30 min, Δz =5 m). Averaging all data in the time series from each area indicates that NoMEF (0.050°C) is slightly warmer than SoMEF (0.043°C). The extremes of mean $\Delta\theta$ in any bin are similar in both areas, with values as low as ~0.034°C and as high as ~0.060°C.

We further visualize the variability of $\Delta\theta$ near MEF by aggregating all data incorporated in Figures 4, 5, and 6 with all data acquired *above* the ridge crests during the same set of stations, sorting into 25 m depth bins, and generating histograms of $\Delta\theta$ for each bin. The resulting distributions of $\Delta\theta$ (Figure 7) characterize the full range of depths (1800–2200 m) influenced by plumes in the vicinities north and south of MEF, and therefore provide some context for Figures 4, 5, and 6 which portray data from only the deepest 4 bins (2100–2200). While the spatial and temporal variability of near-bottom $\Delta\theta$ around the MEF was higher than we expected, the $\Delta\theta$ variance is low in the bottom 100 m relative to the depths above 2100 m, where cross-axis flow increases the variability of plume distributions.

Since Figure 7 combines all of the observations made north or south of the MEF, it can also be used to quantify north–south differences in mean $\Delta\theta$ (hereafter $\overline{\Delta\theta}$). Comparing the bottom 100 m in the north and south, each 25 m bin has a $\overline{\Delta\theta}$ that is greater in the north. The average $\overline{\Delta\theta}$ taken over these 4 deepest bins is 0.063°C in the north, versus 0.056°C in the south.

3.2. Horizontal heat flux estimation

The patchiness of hydrothermal plumes in the axial valley invalidates our initial assumption of thermal heterogeneity, and suggests that unequal lateral fluxes through the different control volume sides are probably commonplace. In the face of this variability, we generate a range of estimates of *mean* heat fluxes by combining the north–south difference in $\overline{\Delta\theta}$ with measurements of v (the along-axis component of flow).

Based on progressive vector diagrams which show that v consistently dominates the across-axis component, heat fluxes through the east and west control surfaces are negligible. With this simplification and the convention that outward fluxes are positive, the net horizontal heat flux (H_h) is the sum of the fluxes through the north and south control surfaces, each of which is normal to v. Thus, H_h represents that fraction of the heat generated by the MEF that leaves the control volume by horizontal advection within 100 m of the sea floor. The remaining fraction of MEF heat passes vertically through the top control surface.

We estimate H_h by multiplying the difference in $\overline{\Delta\theta}$ observed north and south of the MEF by the range of observed along-axis mean velocity ($\overline{v}$), the area of the north or south control surface ($A_h = 3 \times 10^4$ m^2), the reference density (ρ_o), and a heat capacity ($C_p = 4.2$ kJ/kg/°C):

$$H_h = A_h \rho C_p \overline{v}(\overline{\Delta\theta}_N - \overline{\Delta\theta}_S). \qquad (2)$$

Using the north-south difference in $\overline{\Delta\theta}$ values from the bottom 100 m of Figure 7 ($0.063 - 0.056 = 0.007$°C) and a range of observed $\overline{v}$ (+1–5 cm/s), we obtain a range of estimates of H_h: +10–50 MW. Changing the difference $\overline{\Delta\theta}_N - \overline{\Delta\theta}_S$ by 0.001°C changes the value of H_h by 1.25 MW, while increasing the magnitude of $\overline{v}$ by 1 cm/s increases H_h by 10 MW.

The Flow Mow hydrographic survey resolved the MEF temperature field at temporal and spatial scales that are unprecedented. Despite the thermal variability, the north and south control surfaces were sampled frequently enough, and at a wide enough range of tidal phases, to enable estimation of the *mean* net flux, H_h. However, the observations are too sparse and non-synoptic to capture the variations of *instantaneous* net flux out of the control volume. Indeed, given the limitations of the acoustic navigation network and our instruments, it was a grand achievement to assess a single side and a top simultaneously. It was impossible to monitor all 4 sides and the top at once, though that ability is critical if instantaneous fluxes are sought in such variable hydrography. Consequently, we use synthetic data to understand the high variability and interpret our sparse observations.

4. Modeled flux

4.1. Modeled variance and mean magnitudes

To understand the observed hydrographic variability near the MEF and the affect of variable currents on heat flux, we construct a 2-dimensional model of tracer distribution by a point source subjected to a combination of advection and diffusion (Figure 8). Similar "puff" models have been used to understand atmospheric plume distributions [e.g. *Rao et al.*, 1989] and more recently to interpret temperature and current records from moorings near a hydrothermal field [*Wetzler et al.*, 1998; *Lavelle et al.*, 2001]. The model allows the calculation of a $\Delta\theta$ at any point and time in the control volume or on its surfaces.

We force the model with a characteristic oscillation derived through harmonic analysis of the 1995 near-bottom current record. At each time step (1/2 hr), a constant amount of heat (a puff) is added to the 4×4 km model domain from a single source in the middle of the MEF. The puff is thereafter advected by the current, which in this case is purely along-axis and therefore surface-normal. It is also diffused according to a horizontal diffusivity typical of the interior ocean, 0.4 m^2/s [*Okubo*, 1971]. These processes modify the temperature anomalies measured on the surfaces of a ($300 \times 700 \times 100$ m) control volume, generating a time series that can be used to calculate net heat flux through the sides. We then add a range of mean flows to the oscillation to investigate how flux magnitude and variance evolve as the mean flow balances and then exceeds the amplitude of the oscillation.

The model also allows different averaging schemes to be compared. For example, once the temperature field has been recorded at both ends of the control volume for every time step, a feat not yet attainable in the field, the time series can be multiplied by the corresponding current velocities to obtain a series of *instantaneous* net flux across the control surfaces. This flux series may have extraordinarily high variance at low mean flows, but its long-term mean flux must equal the source flux. Alternatively, the temperature series can be averaged before multiplying by the velocity series, or visa versa; this results in *temperature-averaged* or *velocity-averaged* flux series that have variances and means that are different from the instantaneous series.

Figure 9 shows how the means and standard deviations (s) of these 3 types of flux series evolve as the mean flow is incremented in the puff model. The instantaneous mean equals the source flux at mean flows >1 cm/s; at 0 cm/s the mean of the flux series, a product of the zero-mean velocity series, must also be zero, while at $\leqq$1 cm/s the T gradients are so steep that $\sim$5% of the heat diffuses through the control surfaces and is not accounted for. The averaged flux series in the 1–5 cm/s range have mean magnitudes of $\sim$75% of the source flux. This underestimation is due to averaging one of the time series prior to multiplication, and motivates us to adjust our estimates of observed H_h in the next section. The s of the instantaneous flux series is greater than the s of either averaged flux at all flows. In the 1–5 cm/s range of mean flow, the instantaneous s is 1–2$\times$ the source flux magnitude. Expressed as a percentage of the source flux magnitude, the velocity- and temperature-averaged s converge from low-flow values of 150% and 30%, respectively, to $\sim$60% above 2 cm/s. Over the range of typical flows, the model leads to the general expectation that fluxes measured near the MEF will yield averaged flux series with $s \sim 1\times$ the source flux magnitude.

4.2. Model implications for observed flux

Since our estimates of observed H_h are essentially velocity- and temperature-averaged fluxes made in an environment where mean flow is 1–5 cm/s, the model indicates that they should be adjusted upward by a factor of $\sim$1.3 (= 1/0.75). This increases the range of observed H_h from 10–50 MW to $\sim$15–65 MW. Within the same mean flow range, the standard deviation of the modeled averaged flux is $\lesssim$100% of the source flux. Taking the high end of our H_h magnitudes (65 MW) as the source flux that warms the north control surface, the model results suggest that if the Flow Mow experiment were redesigned to monitor both north and south control surfaces simultaneously, then the time series of observed averaged horizontal heat flux would have a maximum s of $\sim$150% of 65 MW, or $\sim$100 MW.

5. Discussion

5.1. Sources of variability in MEF hydrography

The hydrographic patterns observed within the Endeavour axial valley, and particularly the thermal distribution near the MEF, are most likely generated by hydrothermal plumes in a mean northward flow. The puff model shows that tidal pooling and streaming can generate surprisingly heterogeneous plume distributions, especially when forced by a 2-dimensional record (Figure 8), rather than the idealized along-axis oscillation and mean flow. Diffusion and bottom boundary layers will reduce variability over time. These 2 processes appear to balance such that thermal anomalies are present throughout the valley, but are reduced in intensity away from sources. Even midway between known vent fields, plume induced thermal variability rivals that expected from the vertical displacement of isotherms by internal waves [*Veirs*, 2003]. On the periphery of fields the signals are stronger and the heterogeneity increases.

Overall, these competing processes complicate the task of measuring the net flux from a vent field. If mixing rates were greater or there were no mean flow, then the valley would eventually acquire a uniform hydrothermal anomaly that could be more easily inventoried. The observed complexity of the hydrography in the valley suggests that the most successful efforts to measure field-scale fluxes will be those that correctly establish and simultaneously monitor up- and downstream positions over many tidal cycles, or otherwise integrate the variability induced by the tides.

We used both ABE and CTD to monitor the hydrography near the MEF, and endeavored to survey all sides of the control volume at all phases of the tide. Our simple puff model can explain some of the observations, but cannot include many of the possible sources of thermal variability. Even without invoking the possibility of variable source flux (or even fluxes that exhibit tidal variability), multiple constant-flux sources with distinct effluent characteristics (as opposed to the single model source) could enhance variability. Although we have documented that there is significant coherence in the axial currents, small amounts of shear in the velocity field can greatly affect the plume distribution and its variability, with profound ramifications for the potential undersampling of narrow plumes. Finally, a major reason the puff model sometimes fails to explain why one side of the MEF is warmer than the other is the proximity of other heat sources, beyond the perimeter of the control volume. Not only is the diffusely venting Quebec area located nearby, but a major vent field, Mothra, lies upstream of the MEF. The puff model indicates that plumes from either source are likely to be advected intermittently through the MEF.

Despite these numerous complications, plume theory suggests that our survey strategy was optimal for characterizing the average plume distributions near MEF. Plumes from diffuse and focused MEF sources are expected to bend over in the axial cross flows and equilibrate within the depth range we monitored. To prevent equipment damage, we avoided the bottom 5–10 m of each side, but based on knowledge of the source fluids within the MEF, we expect that the lateral flux of heat through this gap is small compared to that through the 5–100 mab range.

While it is possible that a low B vent could produce a plume that hugs the sea floor [e.g. *Trivett and Williams*, 1994] and is advected beyond the field through the gap, during the summer of 2000, all MEF sources had negative salinity anomalies (ΔS): -9 to -14‰ for high B sources in the south part of MEF; -4 to -8‰ in northern high B vents; and about -0.5‰for low B vents in general (D. Butterfield, pers. comm.). Numerical models of diffuse plume rise (J.W. Lavelle, pers. comm., see caption of Figure 8) indicate that in typical stratifications, vents with negative ΔS, no matter the magnitude of their positive source $\Delta\theta$, will produce plumes that separate from the sea floor downstream of the source. When the source properties (measured S and T, and estimated w and A) are used to quantify a range of B for MEF low T vents, and the results are used to initialize the plume rise models (along with a reasonable range of environmental conditions, namely the buoyancy frequency, N, and cross flow velocity, U), the range of expected rise heights and plume thicknesses creates significant temperature anomalies at elevations of 15–35 m for $\Delta S = +0.5$‰ and 20–90 m for $\Delta S = -0.5$‰. In cross flow of 5 cm/s the modeled plumes equilibrate $\lesssim$250 m downstream of their source. These predictions suggest that low B, negative ΔS MEF plumes may actually rise up through the top surface of the control volume on their own accord unless they are first carried through a side surface by cross flow or entrained by high B plumes.

If currents of $\sim$5 cm/s orthogonal to the sides are assumed to generate variability on time scales of $\sim$1000 s (the time it took ABE or the CTD to complete a lap horizontally or vertically), then the characteristic dimension of thermal patches would be about 50 m, an estimate that is in rough agreement with the smallest scale of variation observed on any individual pass. This is also the approximate scale of the smallest features generated by a numerical model of a typical MEF diffuse plume (J.W. Lavelle, pers. comm.).

The behavior of focused hydrothermal plumes in uniform cross flow has been modeled both analytically [*Middleton and Thomson*, 1986] and numerically [*Lavelle*, 1997]. With some approximation of the typical in-valley stratification, plumes from MEF focused sources (with the observed range of source S and T) are expected to rise anywhere from 200 m in nearly quiescent conditions (1 cm/s cross flow) to 100 m in typical peak MEF cross flows of 10 cm/s. Although measurements of 20 cm/s peak cross flows are rare in the 1995 and 2000 records (~1 event in 20 days), plume rise during such flow could be reduced to ~50 m.

The surprisingly small-scale heterogeneities observed on the sides of the MEF likely originate when diffuse sources with different B and depth (10–15 m vertical separation) vent into a mean cross flow, generating plumes with distinct rise heights. When tidal oscillations also influence the dynamics and distribution of plumes, high temporal variability becomes the norm, especially when observations are made close to the hydrothermal sources. During peak cross flows, even plumes from high B sources may transit the upper 1/2 of the sides of the control volume.

5.2. Implications for vertical heat flux calculation

The heterogeneous hydrography observed within the axial valley implies that the fluid entrained by rising MEF plumes can have variable heat content. This complicates the interpretation of the heat flux measurements made on the top surface of the Flow Mow control volume because relating measured anomalies to source heat flux through 1-

dimensional plume theory requires an assumption of a linear background θ–S relationship in the entrained fluid.

However, the consistent northward flow within the axial valley means that fluid entrained by MEF plumes enters the field predominantly through the south side of the control volume. As detailed in [*Stahr et al.*, submitted, 2002], a viable approach is to average all $\Delta\theta$ estimates from the area south of the MEF and subtract the result ($\overline{\Delta\theta}_S \simeq 0.05°\mathrm{C}$) from each of N observations of $\Delta\theta$ made on the top surface (with area, A_v) by ABE to calculate the vertical heat flux (H_v) as

$$H_v = A_v \rho C_p \sum_{i=1}^{N} w_i (\Delta\theta_i - \overline{\Delta\theta}_S), \tag{3}$$

where w is vertical velocity. This is equivalent to assuming that fluid entrained at any depth within 100 mas has the same average T and S, which is partially justified by the observation of intermittent well-mixed layers < 50 mab. Additionally, during horizontal CTD tows through the MEF at depths of 30–60 mas, the $\Delta\theta$ between buoyant plumes is typically $0.05 \pm 0.01°\mathrm{C}$. Altering the value of $\overline{\Delta\theta}_S$ by $0.01°C$ changes the vertical flux estimate by $\sim$10 MW.

5.3. Partitioning heat flux between MEF sources

The Flow Mow experimental results can be combined with past measurements in a heat budget to infer how MEF heat flux is partitioned between focused and diffuse vents. We first assume that the total flux through the sea floor into the control volume is the sum of the flux through focused sources (H_f) and the flux through diffuse sources (H_d). Similarly, we take the total flux out of the MEF control volume to be the sum of the vertical flux through the top (H_v) and the horizontal flux through the sides (H_h). This leads to an expression for the steady state heat budget:

$$H_d + H_f + H_v + H_h = 0. \tag{4}$$

As indicated previously for H_h (Equation 2) and H_v (Equation 3), we treat $\overline{\Delta\theta}_S$ as a reference temperature anomaly, subtracting it from the measured $\Delta\theta$ in each of the H terms in Equation 4. Making this adjustment, and following the outward flux sign convention, estimates of H_f range from about −350 MW [*Ginster et al.*, 1994] to roughly −200 MW [*Bemis et al.*, 1993]. With attention to the uncertainties involved in the 2 studies, a reasonable estimate of H_f is −300 MW. The mean value of H_v is about +550 MW [*Stahr et al.*, submitted, 2002] while H_h is approximately +65 MW. Solving Equation 4 for H_d and dividing both sides by H_f, the ratio of diffuse to focused flux becomes

$$\frac{H_d}{H_f} = \frac{-(H_f + H_v + H_h)}{H_f} = \frac{-(-300 + 550 + 65)}{-300} = \frac{-315}{-300}. \tag{5}$$

Thus, MEF heat flux is partitioned about equally between diffuse and focused sources, that is $H_d \simeq H_f \simeq 300$ MW. This constitutes a revision of the idea that diffuse flux dominates focused flux in a ratio of about 10:1 [*Schultz et al.*, 1992]. If we assume that only diffuse sources are responsible for the observed horizontal flux, then an additional implication of H_h having a magnitude of $\lesssim 65$ MW is that roughly 4/5 of H_d is entrained into rising plumes within the MEF perimeter, while only $\sim 1/5$ escapes the field laterally.

5.4. Future directions

The Flow Mow experiment, through both its vertical and horizontal components, improved the precision of heat flux measurements made at the field scale. The same methodology could be applied at other fields along the Endeavour segment and the results summed to obtain a segment-scale flux. Such an effort could take advantage of the mean northward flow within the axial valley to quantify horizontal fluxes between fields. Instrumenting a segment would help to discern whether near-bottom heat is exported laterally below the equilibrium depths, vertically through entrainment in higher-rising plumes, or both. An outstanding question is whether all heat within the axial valley is ultimately entrained, and thereby integrated, by high B plumes. Effluent with a positive ΔS is least likely to be entrained [*Turner and Campbell*, 1987]; near the sources of such fluid it will be particularly critical to monitor the near-bottom environment for lateral fluxes.

At segments where the topography of the axial valley does not rectify deep sea oscillations, synoptic and precise measurement of the horizontal flux from a field may be very difficult. In unconstrained and often rotary flow, long time series will be required to achieve accurate mean fluxes [*Thomson et al.*, 1992], while meaningful instantaneous fluxes will only be obtained if all sides of a control volume are monitored, ideally through a strategy guided by advection/diffusion models that predict the evolution of the T field.

6. Acknowledgments

This work was supported through NSF grant OCE-9872090. Special thanks to Christian Sarason Parker and the REVEL 2000 participants, who acquired 179 hr of CTD data in just over 2 weeks. This exceptional resolution of the MEF hydrography was also made possible by the (ABE) engineering genius of Dana Yoeger, Al Bradley, and their WHOI collaborators, as well as the captain, marine technicians, and crew of the R/V Thompson who patiently cycled the ship and CTD around the MEF control volume. Rick Thomson and his team at the Institute for Ocean Science, Canada deployed, recovered, and processed all current meter moorings and generously provided the northern meter record. Meg Tivey graciously made her MAVS data available for comparison. We greatly appreciate many helpful discussions and reviews with Bill Lavelle, who also provided numerical simulations of MEF diffuse plumes. Figure generation, modeling, and typesetting were accomplished with GMT [*Wessel and Smith*, 1991], Matlab, and LaTeX.

References

Baker, E. T., and G. J. Massoth, Characteristics of hydrothermal plumes from two vent fields on the Juan de Fuca Ridge, northeast Pacific Ocean, *Earth Planet. Sci. Lett.*, *85*, 59–73, 1987.

Bemis, K. G., R. P. von Herzen, and M. J. Mottl, Geothermal heat flux from hydrothermal plumes on the Juan de Fuca ridge, *J. Geophys. Res.*, *98*, 6351–6369, 1993.

Delaney, J. R., V. Robigou, R. E. McDuff, and M. K. Tivey, Geology of a vigorous hydrothermal system on the Endeavour segment, Juan de Fuca ridge, *J. Geophys. Res.*, *97*, 19,663–19,682, 1992.

Delaney, J. R., M. Lilley, R. E. McDuff, D. Kelley, W. Wilcock, and V. Robigou, Cellular hydrothermal circulation in a submarine system, *Eos. Trans. AGU*, *77*, 756, 1996.

Elvers, D., S. Srivastava, K. Potter, J. Morley, and D. Solidel, Asymmetric spreading across the Juan de Fuca and Gorda rises as obtained from a detailed magnetic survey, *Earth Planet. Sci. Lett.*, *20*, 211–219, 1973.

Franks, S., *Temporal and spatial variability in the Endeavour ridge neutrally buoyant hydrothermal plume: Patterns, forcing mechanisms and biogeochemical implications*, University of Washington, Seattle, USA, 1992.

Ginster, U., M. J. Mottl, and R. P. Von Herzen, Heat flux from black smokers on the Endeavor and Cleft segments, Juan de Fuca ridge, *J. Geophys. Res.*, *99*, 4937–4950, 1994.

Johnson, H., et al., Survey studies hydrothermal circulation on the northern Juan de Fuca Ridge, *Eos Trans. AGU*, *83*, 73–79, 2002.

Kappel, E., and W. Ryan, Volcanic episodicity and a nonsteady rift valley along northeast Pacific spreading centers: Evidence from SeaMARCI, *J. Geophys. Res.*, *91*, 13,925–13,940, 1986.

Keller, G. H., S. H. Anderson, and J. W. Lavelle, Near-bottom currents in the Mid-Atlantic Ridge rift valley, *Can. J. Earth Sci.*, *12*, 703–710, 1975.

Kelley, D., J. Baross, and J. Delaney, Volcanoes, fluids, and life in submarine environments, *Annu. Rev. Earth Planet. Sci.*, *30*, 385–491, 2002.

Lavelle, J. W., Buoyancy-driven plumes in rotating, stratified cross flows: Plume dependence on rotation, turbulent mixing, and cross-flow strength, *J. Geophys. Res.*, *102*, 3405–3402, 1997.

Lavelle, J. W., E. T. Baker, and G. J. Massoth, On the calculation of total heat, salt and tracer fluxes from ocean hydrothermal events, *Deep Sea Res., Part II*, *45*, 2619–2636, 1998.

Lavelle, J. W., M. A. Wetzler, E. T. Baker, and R. W. Embley, Prospecting for hydrothermal vents using moored current and temperature data: Axial Volcano on the Juan de Fuca ridge, northeast Pacific, *J. Phys. Ocean*, *31*, 827–838, 2001.

McDougall, T. J., Bulk properties of “hot smoker” plumes, *Earth Planet. Sci. Lett.*, *99*, 185–194, 1990.

McDougall, T. J., and K. G. Speer, Fluxes of heat and tracers in “hot smoker” plumes, *J. Geophys. Res.*, *104*, 18,301–18,304, 1999.

McDuff, R. E., Physical dynamics of deep-sea hydrothermal plumes, in *Seafloor Hydrothermal Systems: Physical, Chemical, Biological, and Geological Interactions*, edited by S. E. Humphris, R. A. Zierenberg, L. S. Mullineaux, and R. E. Thomson, pp. 357–368, American Geophysical Union, 1995.

Middleton, J. H., and R. E. Thomson, Modeling the rise of hydrothermal plumes, *Can. Tech. Rep. Hydrog. Ocean. Sci.*, *69*, 1–18, 1986.

Morton, B. R., Forced plumes, *J. Fluid. Mech.*, *5*, 151–163, 1959.

Murton, B., L. Redbourn, C. German, and E. Baker, Sources and fluxes of hydrothermal heat, chemicals and biology within a segment of the Mid-Atlantic ridge, *Earth Planet. Sci. Lett.*, *171*, 301–317, 1999.

Okubo, A., Oceanic diffusion diagrams, *Deep-Sea Research*, *18*, 789–802, 1971.

Rao, K. S., R. M. Eckman, and R. Hosker, Simulation of tracer concentration data in the Brush Creek drainage flow using an integrated puff model, *Journal of Applied Meteorology*, *28*, 609–616, 1989.

Rudnicki, M. D., R. H. James, and H. Elderfield, Near-field variability of the TAG non-buoyant plume, 26°n, Mid-Atlantic Ridge, *Earth Planet. Sci. Lett.*, *127*, 1–10, 1994.

Schultz, A., J. R. Delaney, and R. E. McDuff, On the partitioning of heat flux between diffuse and point source seafloor venting, *J. Geophys. Res.*, *97*, 12,299–12,314, 1992.

Speer, K. G., and P. A. Rona, A model of an Atlantic and Pacific hydrothermal plume, *J. Geophys. Res.*, *94*, 6213–6220, 1989.

Stahr, F. R., R. E. McDuff, and S. R. Veirs, Vertical heat flux at the Main Endeavour field, *Geochem. Geophys. Geosyst.*, submitted, 2002.

Thomson, R. E., J. R. Delaney, R. E. McDuff, D. R. Janecky, and J. S. McClain, Physical characteristics of the Endeavour ridge hydrothermal plume during July 1988, *Earth Planet. Sci. Lett.*, *111*, 141–154, 1992.

Thomson, R. E., S. F. Mihaly, A. B. Rabinovich, R. E. McDuff, S. R. Veirs, and F. R. Stahr, Topographically constrained circulation at Endeavour ridge: Implications for the colonization of hydrothermal vent fields, *Science*, submitted, 2002.

Thurnherr, A., K. Richards, C. German, G. Lane-Serff, and K. Speer, Flow and mixing in the rift valley of the mid-atlantic ridge, *Journal of Physical Oceanography*, *132*, 1763–1778, 2002.

Thurnherr, A. M., *Hydrography and flow in the rift valley of the Mid-Atlantic ridge*, University of Southampton, England, 2000.

Trivett, D. A., and A. J. Williams, Effluent from diffuse hydrothermal venting. 2. Measurements of plumes from diffuse hydrothermal vents at the southern Juan de Fuca Ridge, *J. Geophys. Res.*, *99*, 18,417–18,432, 1994.

Turner, J. S., and I. H. Campbell, Temperature, density and buoyancy fluxes in “black smoker” plumes, and the criterion for buoyancy reversal, *Earth Planet. Sci. Lett.*, *86*, 85–92, 1987.

Veirs, S. R., *Submarine volcanic heat flux and hydrography: observations and models of the Main Endeavour vent field in the northeast Pacific*, University of Washington, Seattle, WA, USA, 2003.

Veirs, S. R., R. E. McDuff, M. D. Lilley, and J. R. Delaney, Locating hydrothermal vents by detecting buoyant, advected plumes, *J. Geophys. Res.*, *104*, 29,239–29,247, 1999.

Wessel, P., and W. Smith, Free software helps map and display data, *EOS Trans. AGU*, *72*, 441, 1991.

Wetzler, M. A., J. W. Lavelle, G. A. Cannon, and E. T. Baker, Variability of temperature and currents measured near Pipe Organ hydrothermal vent site, *Mar. Geophys. Res.*, *20*, 505–516, 1998.

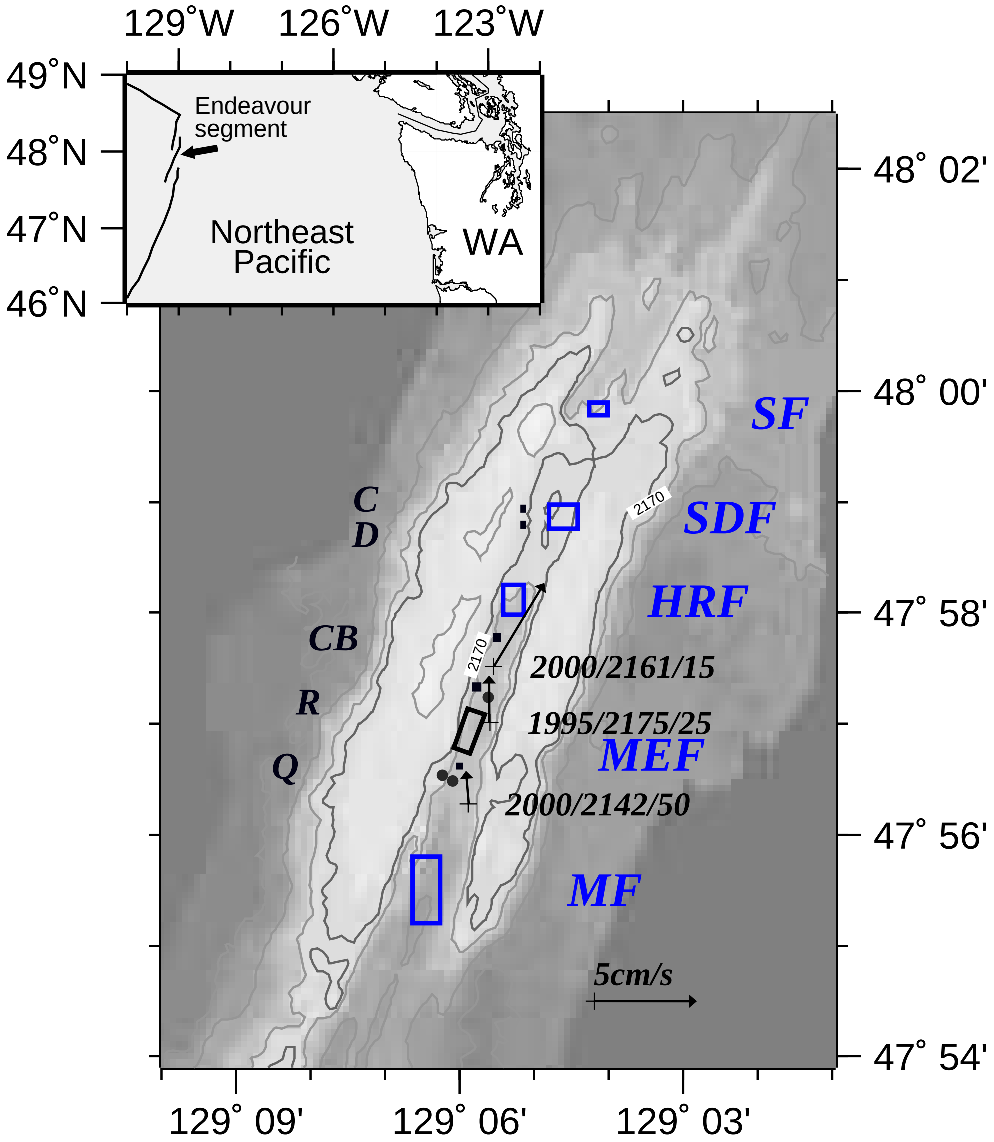

Figure 1. Endeavour segment bathymetric map showing known hydrothermal sources: open boxes are major fields (MF=Mothra, MEF=Main, HRF=High Rise, SDF=Salty Dawg, SF=Sasquatch) and small solid squares are diffuse or isolated focused vents (Q=Quebec, R=Raven/ReddFox, CB=Clam Bed, D=Dune, C=Cirque). Contours are every 100 m and 2170 m. Inset map locates segment on Juan de Fuca ridge. Mean current vectors superimposed on mooring locations (+) labeled (year,depth,elevation); 5 cm/s vector scale at lower right. Open black box aligned with ridge axis is perimeter of MEF and Flow Mow control volume. Solid circles (●) are CTD monitoring stations (NoMEF and SoMEF).

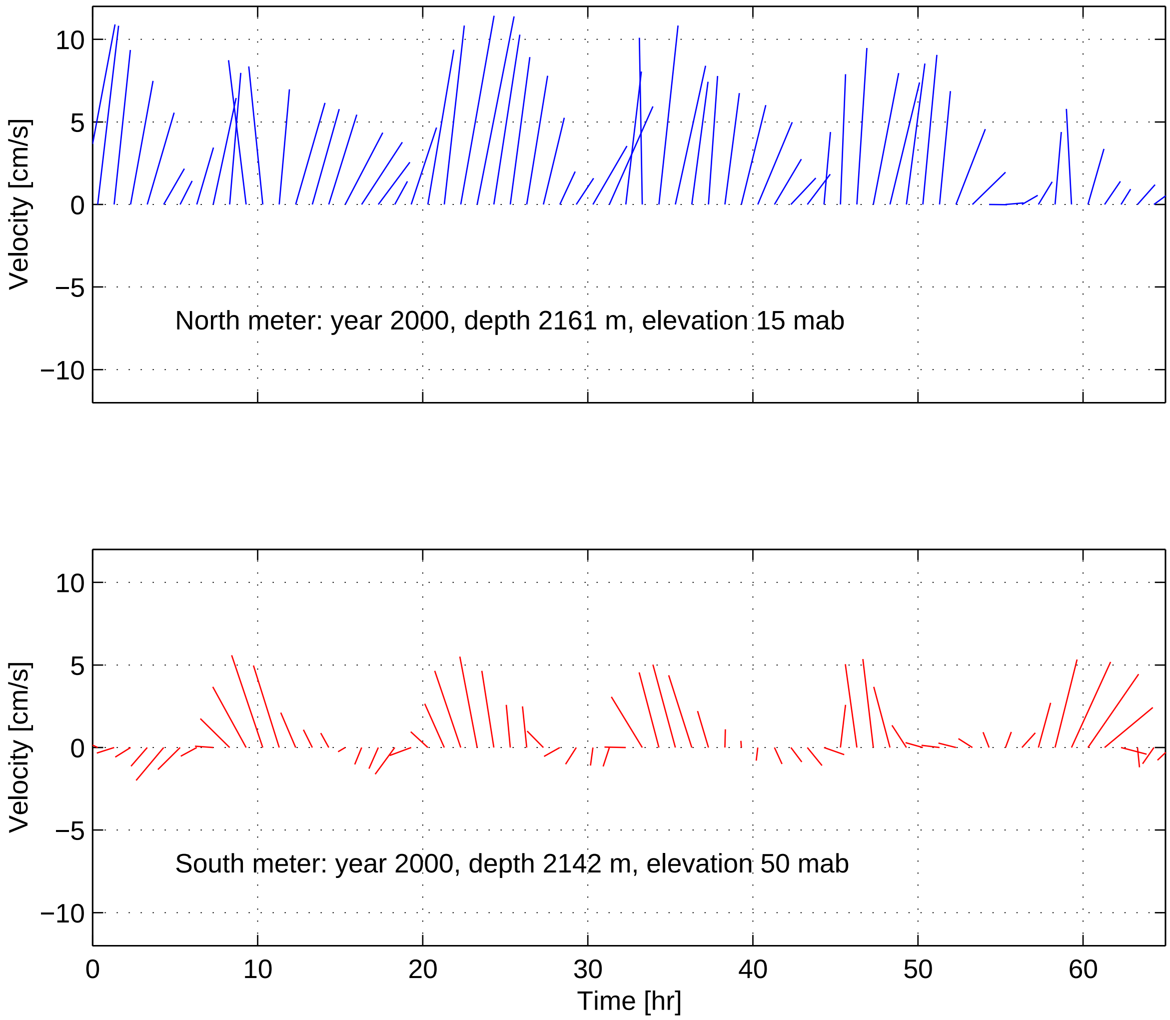

Figure 2. A 65 hr time series of hourly-mean currents within the axial valley north (top) and south (bottom) of the MEF. True north is up.

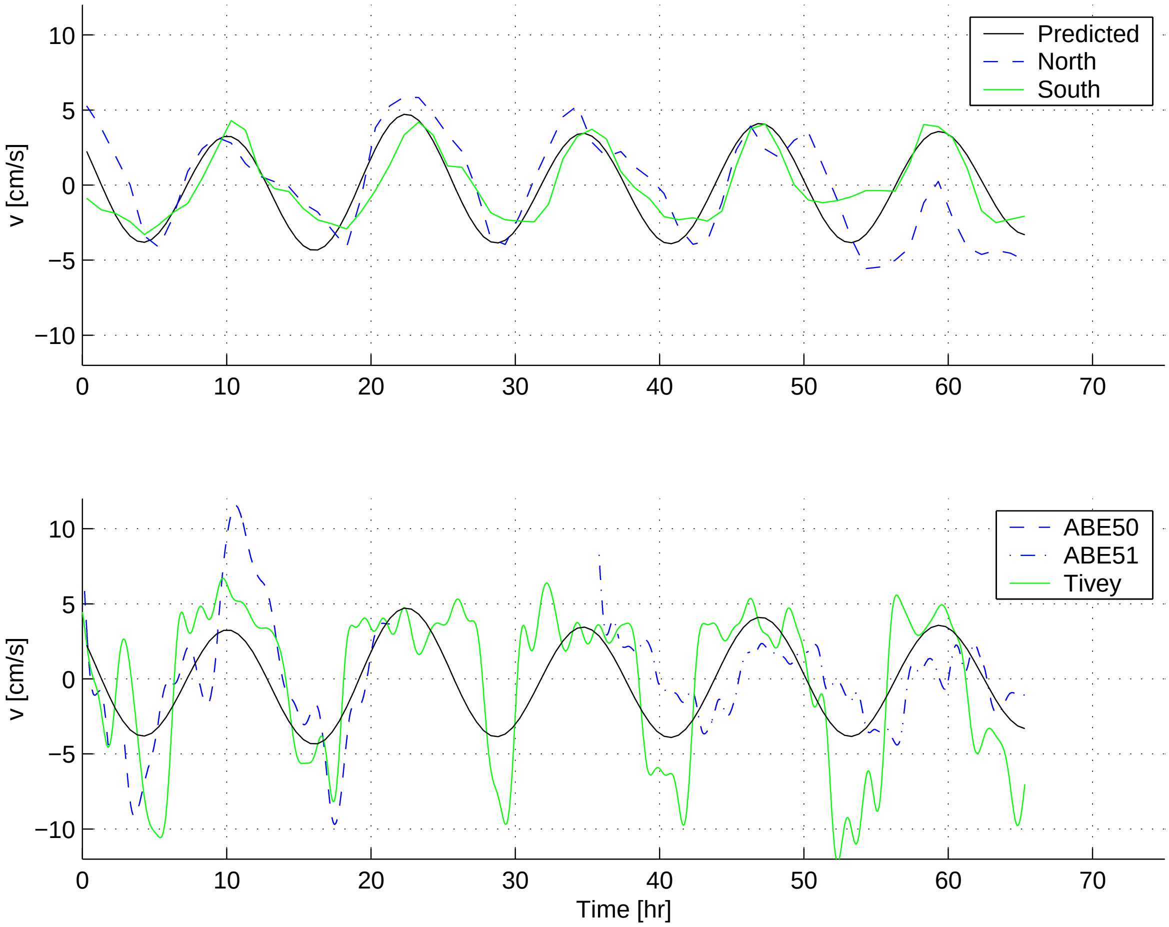

Figure 3. The zero-mean, along-axis component of flow measured at the north and south moorings (top) and at the MEF (bottom), recorded during the same period as in Figure 2. Each is referenced to the flow extrapolated to the year 2000 through harmonic analysis (H. Mofjeld, pers. comm.) using 60 days of 10 min mean data acquired 25 mab at the northeast corner of the MEF in 1995. Time series in the lower panel are from: a MAVS deployed by M. Tivey ~0.5 mab near the center of the MEF, about 40 m north of the S&M sulfide structure; a MAVS mounted on ABE during the 2 longest dives (ABE50 and ABE51). All MAVS data were smoothed with Butterworth low pass filters.

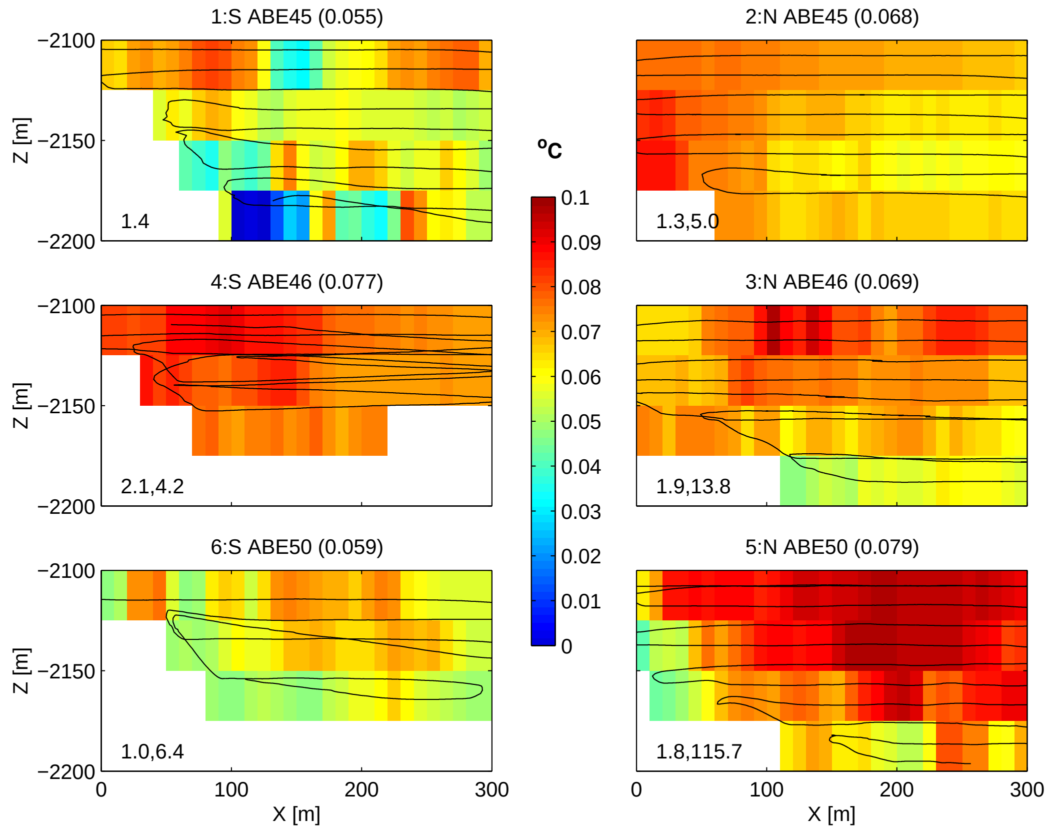

Figure 4. Spatially averaged $\Delta\theta$ from ABE dives 45, 46, and 50 projected orthogonally onto south and north control surfaces. Black line is ABE track. Different maximum survey depths are due to tuning of ABE's bottom-avoidance algorithm. Averaging bins are 10 m wide and 25 m high. White areas have no data. The title begins with a number indicating the order in which the surfaces were surveyed and ends with the mean of all bins (noted parenthetically). Annotations in lower left corner of each panel are duration of that surface, followed by time since the end of the previous surface, both in hours.

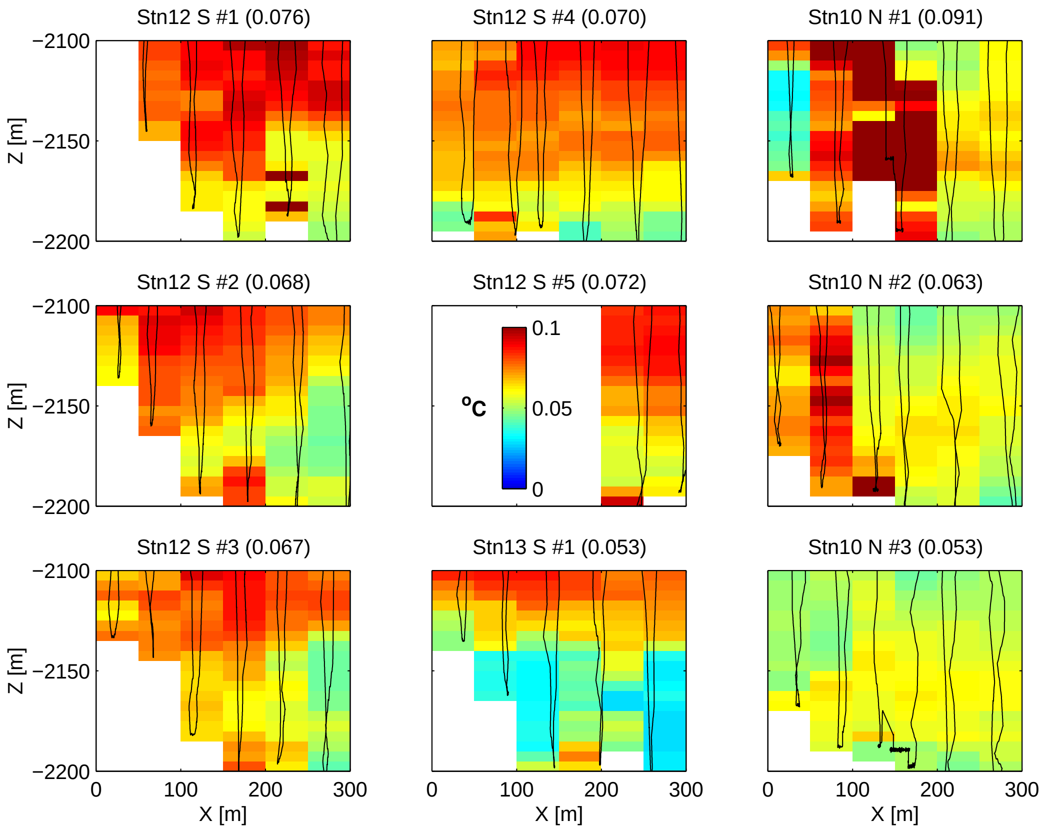

Figure 5. Spatially averaged $\Delta\theta$ from CTD stations 10, 12, and 13 projected orthogonally onto south (S) and north (N) control surfaces. Black line is CTD track. Averaging bins are 100 m wide and 5 m high. Mean of all bins is noted parenthetically for each surface. White areas have no data. Bottoms of successive vertical oscillations are spaced ~20 min apart; most surfaces were surveyed in 80–100 min. Station 12 began ~3.8 hr after station 10 ended, and station 13 began ~14.2 hr after the end of station 12.

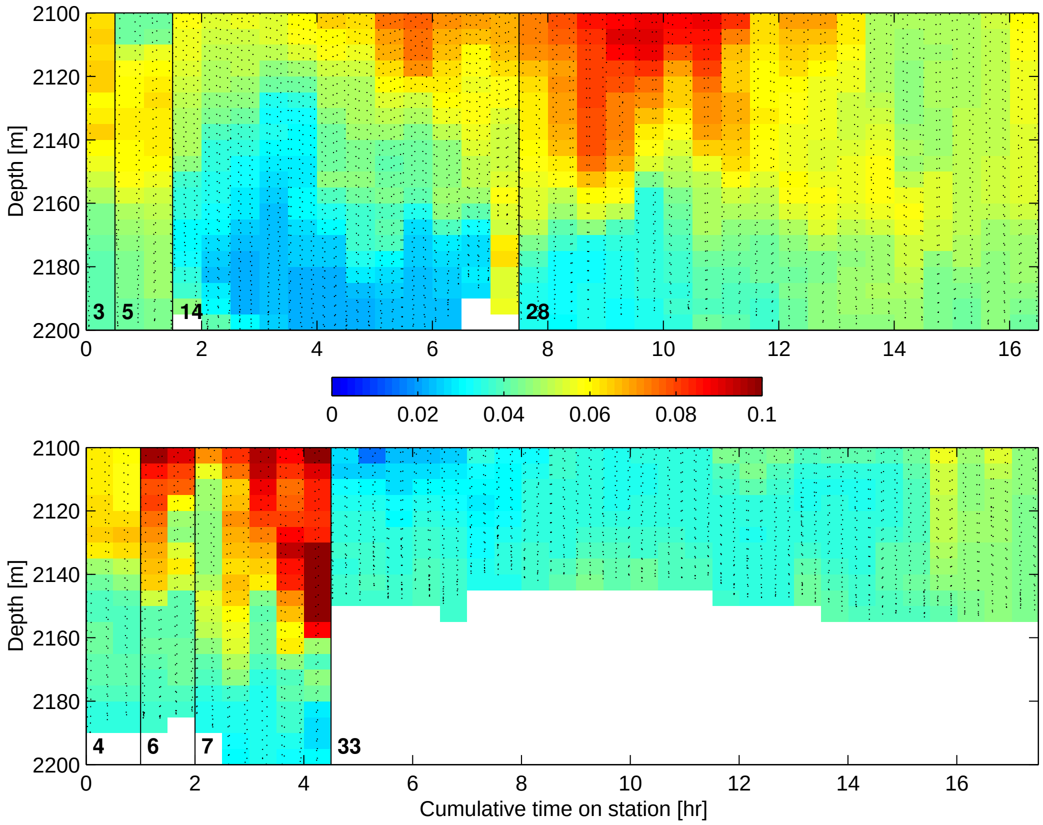

Figure 6. Time series of spatially and temporally averaged $\Delta\theta$ from CTD and ABE surveys of the NoMEF and SoMEF areas. Dotted black line is CTD track. Averaging bins are 1/2 hr wide and 5 m high. Vertical black lines mark temporal breaks (~1-5 days) between stations, each of which is numbered in lower left corner. White areas have no data. Station 33 does not extend below 2155 m because it was located west of stations 4, 6, and 7, where the western scarp shoals to ~2160 m (see dual SoMEF locations, Figure 1).

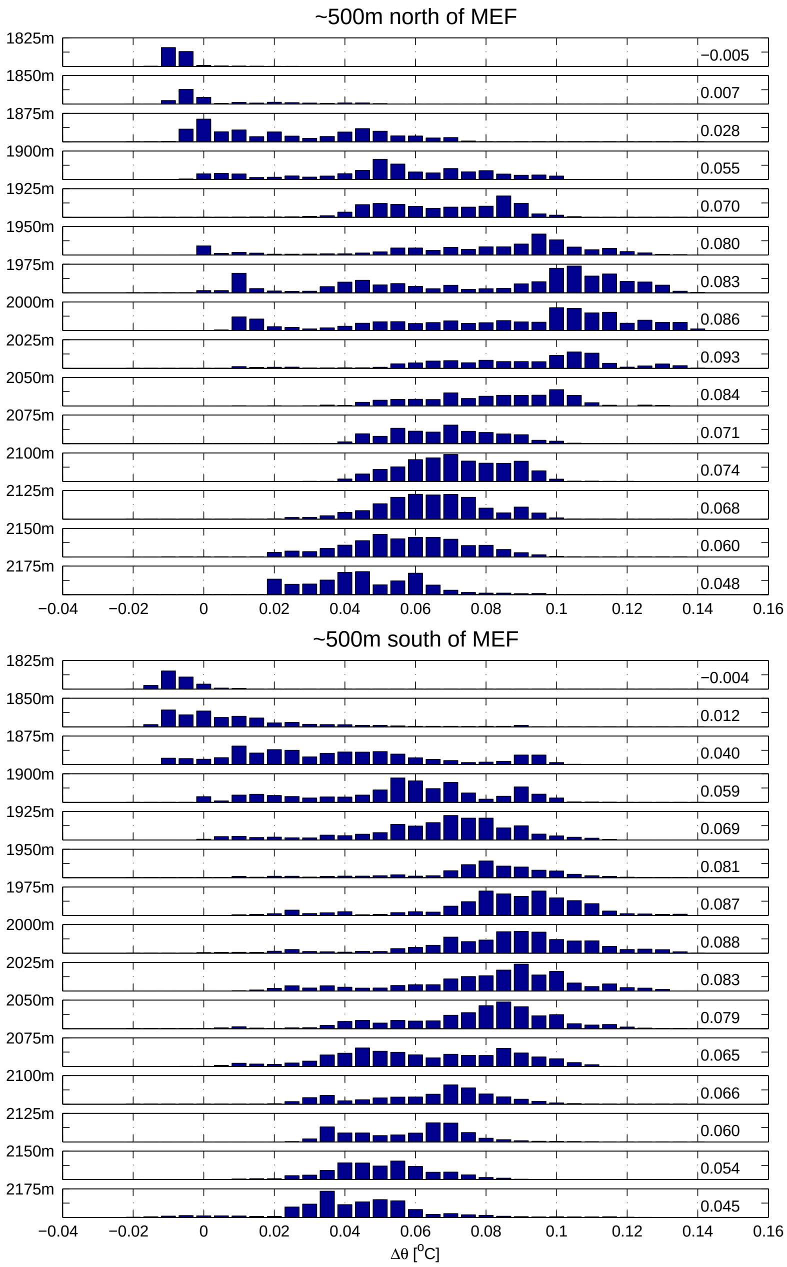

Figure 7. Stacked histograms of depth-binned $\Delta\theta$ observed north (upper) and south (lower) of the MEF. Depth range of each bin is 25 m and upper extent of each bin is noted on the left axis. For reference, the nearby ridge crests have a mean depth of ~2100–2125 m. $\Delta\theta$ for each distribution is tabulated at right. North data is from CTD stations 3, 5, 10, 14, and 28, and ABE dives 45, 46, and 50; south data is from CTD stations 4, 6, 7, 12, 13, and 33, and ABE dives 45, 46, 50.

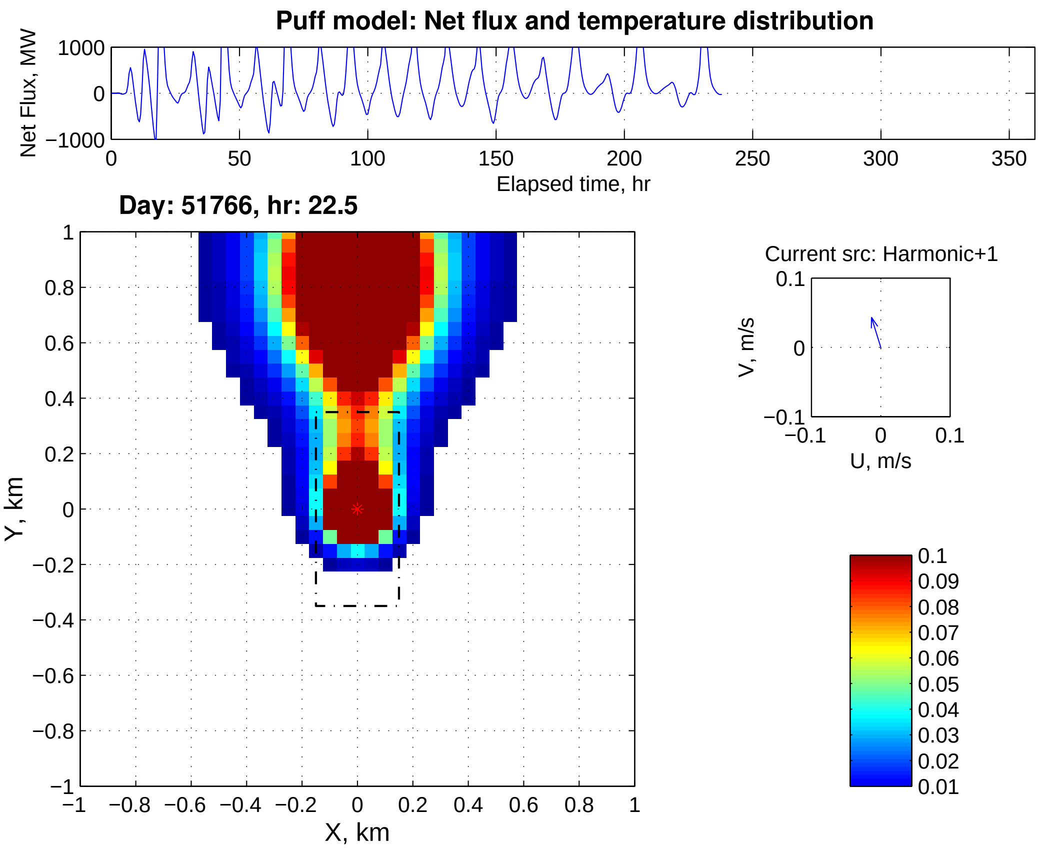

Figure 8. A single frame from a puff model animation showing a plan view of the distribution of temperature around the MEF (black box). In this snapshot, the model is forced by the idealized flow (harmonic analysis + 1 cm/s mean) and the source flux is constant (300 MW). Smaller panels show the instantaneous net flux through the MEF perimeter, the half-hourly current vector, and a colorbar with temperature anomaly units in °C. Animations of the puff model and Bill Lavelle's diffuse plume model have been submitted as supplementary material, and may be presented through a web page akin to the temporary prototype that can be accessed via the authors' website: econscience.org/scott/g3/

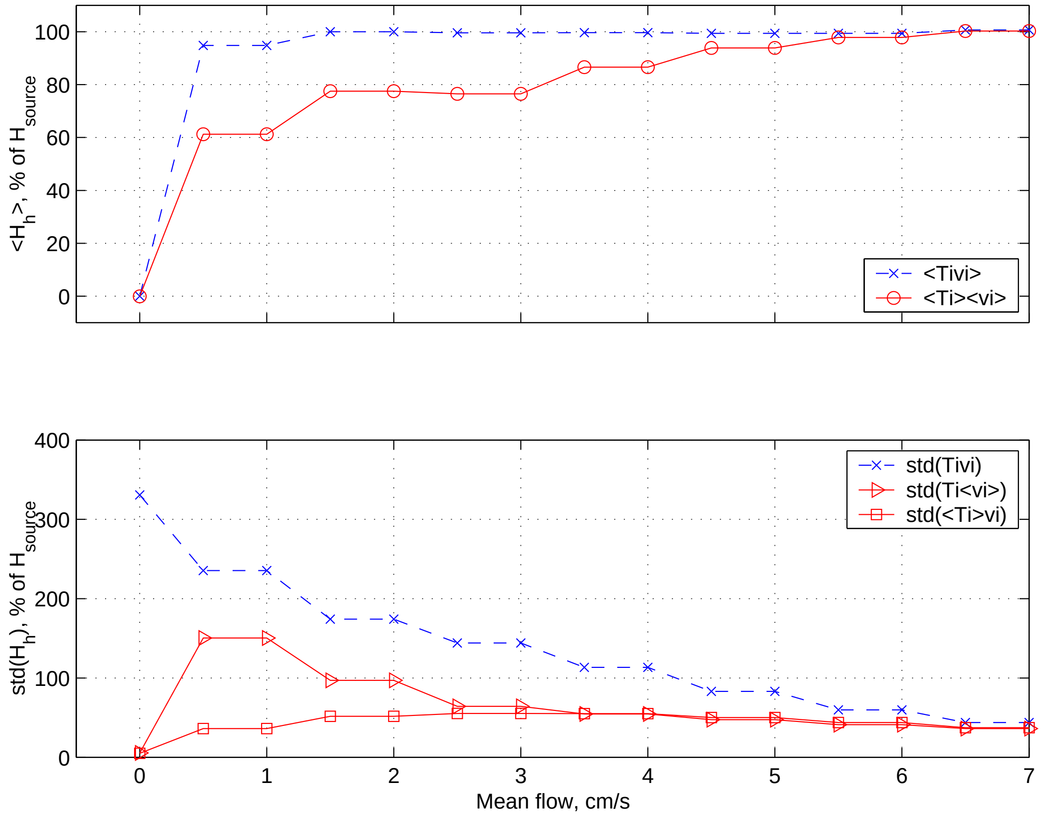

Figure 9. Means and standard deviations of horizontal flux (H_h) series modeled over a range of mean flows, expressed as percentage of source heat flux (H_{source}). Upper panel shows the means for instantaneous (<Tivi>) and averaged (<Ti><vi>) flux series. Lower panel shows standard deviations of instantaneous (Tivi), velocity-averaged (Ti<vi>), and temperature-averaged (<Ti>vi) flux series.